Strong and Tunable Spin-Lifetime Anisotropy in Dual-Gated Bilayer Graphene

Jinsong Xu, Tiancong Zhu, Yunqiu Kelly Luo, Yuan-Ming Lu, and Roland K. Kawakami

Phys. Rev. Lett. **121**, 127703 — Published 20 September 2018

DOI: 10.1103/PhysRevLett.121.127703

Strong and Tunable Spin Lifetime Anisotropy in Dual-Gated Bilayer Graphene

Jinsong Xu, Tiancong Zhu, Yunqiu Kelly Luo, Yuan-Ming Lu, and Roland K. Kawakami

Department of Physics, The Ohio State University, Columbus, OH 43210, USA

ABSTRACT

We report the discovery of a strong and tunable spin lifetime anisotropy with excellent out-of-plane spin lifetimes up to 7.8 ns at 100 K in dual-gated bilayer graphene. Remarkably, this realizes the manipulation of spins in graphene by electrically-controlled spin-orbit fields, which is unexpected due to graphene's weak intrinsic spin-orbit coupling (~12 μeV). We utilize both the in-plane magnetic field Hanle precession and oblique Hanle precession measurements to directly compare the lifetimes of out-of-plane vs. in-plane spins. We find that near the charge neutrality point, the application of a perpendicular electric field opens a band gap and generates an out-of-plane spin-orbit field that stabilizes out-of-plane spins against spin relaxation, leading to a large spin lifetime anisotropy (defined as the ratio between out-of-plane and in-plane spin lifetime) up to ~12 at 100 K. This intriguing behavior occurs because of the unique spin-valley coupled band structure of bilayer graphene. Our results demonstrate the potential for highly tunable spintronic devices based on dual-gated 2D materials.

Graphene is an outstanding material for spin transport because its low spin-orbit coupling (SOC) [1-3] leads to record long spin diffusion lengths at room temperature [4-6]. However, such weak SOC makes it difficult to electrically control spins in graphene, which is highly desired for spintronic device operation [7-10]. Therefore, attention has focused on utilizing stacked heterostructures for graphene spintronics [11-29]. For example, experiments have shown that adjacent ferromagnetic insulator layers can strongly modulate spin currents via proximity exchange fields [11-16], while adjacent transition metal dichalcogenide (TMDC) layers enable the optical injection of spin [17,18] and electrical modulation of spin currents via spin absorption [19,20]. More recently, groundbreaking measurements of large spin lifetime anisotropy (comparing lifetimes of out-of-plane vs. in-plane spins) in graphene-TMDC heterostructures have unambiguously identified the presence of proximity-induced SOC and its impact of spin transport in graphene [25,26]. While this holds great promise for the electrical control of spins in graphene, the observed spin lifetimes in these heterostructures are short (<50 ps) due to the relatively strong SOC in TMDCs.

In this Letter, we report the remarkable observation of a strong and tunable spin lifetime anisotropy in dual-gated bilayer graphene (BLG) with spin lifetimes up to 7.8 ns. The strong spin lifetime anisotropy is unexpected due to graphene's weak intrinsic SOC, but occurs because applying a perpendicular electric field breaks the inversion symmetry of Bernal-stacked BLG, which opens a band gap and dramatically alters the character of the SOC [30-33]. Our experiments are performed on BLG lateral spin valves with top and bottom gates to independently control the perpendicular electric field and carrier density. The spin lifetime anisotropy ($\xi = \tau_{\perp}/\tau_{\parallel}$ where $\tau_{\perp}$ ($\tau_{\parallel}$) is the lifetime for spins oriented out-of-plane (in-plane)) is determined by means of both in-plane magnetic field Hanle and oblique Hanle measurements [25,26]. We observe strong anisotropy (ξ up to 12.2) near the charge neutrality point (CNP) when an electric field is applied. A detailed study shows that ξ increases with applied electric field. This behavior is observed in two samples, one of which saturates around 0.5 V nm^{-1} and eventually decreases. This intriguing behavior can be explained by the unique band structure of BLG [32,33] where an electric field tunes the gap, and the band edges have spin-orbit splitting (tens of μeV) and spin-valley coupling similar to TMDCs [34]. This produces gate-tunable effective spin-orbit fields that protect out-of-plane spins from dephasing by Dyakonov-Perel spin relaxation. These results demonstrate strong and gate-tunable spin lifetime anisotropy with excellent spin lifetime in BLG, which provides a prototype 2D system for next generation spintronic devices based on electrical control of effective spin-orbit fields.

Spin valve devices (Figure 1a) are fabricated by exfoliating and stacking layers of BLG and hexagonal boron nitride (h-BN) onto a Si wafer with 300 nm SiO_2 overlayer. For the bottom gate, we utilize the highly p-doped Si wafer as a global backgate with the 300 nm SiO_2 serving as the gate dielectric. For the top gate, we utilize a patterned Cr/Au electrode separated from the BLG by an h-BN dielectric layer. For spin transport, non-magnetic Cr/Au electrodes (E1, E4, both ~ 1 kΩ) are used as reference contacts and Co electrodes with SrO tunneling barriers [35] (E2 ~ 22.8 kΩ, E3 ~3.7 kΩ) are used for spin injection and detection. Details of device fabrication are provided in the Supplemental Material (SM) section S1 [36-38].

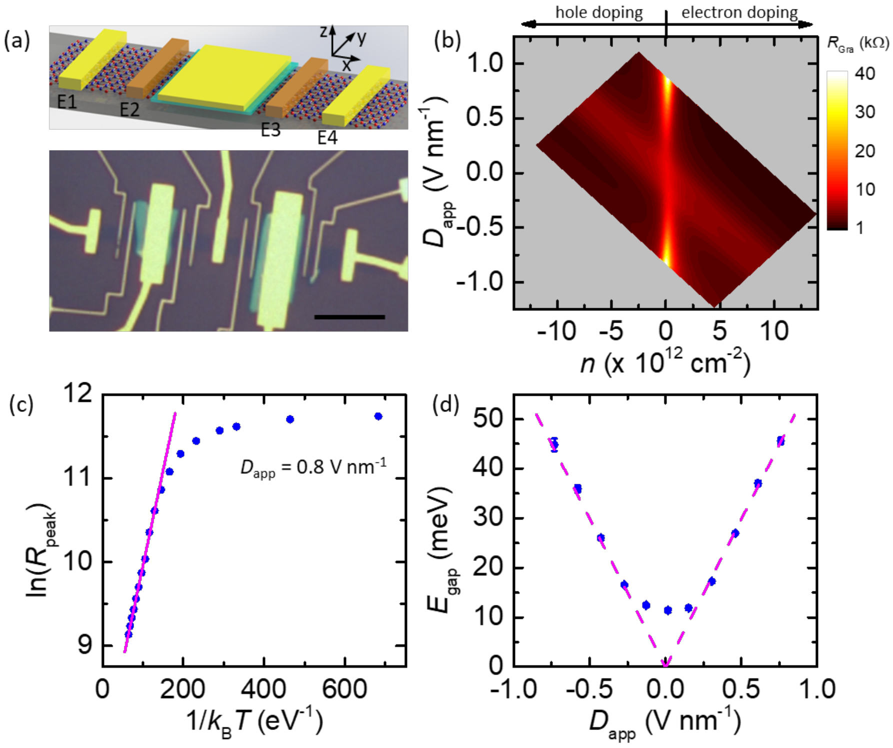

FIG. 1. (a) (Top) Schematic of the device. Yellow: Cr/Au electrode, Brown: Co electrode, Cyan: h-BN, Grey: SiO_2. (Bottom) Optical image of a BLG spin valve. The scale bar is 10 µm. (b) Electric field and carrier density dependent BLG resistance. (c) Temperature dependent BLG channel peak resistance R_{peak} at D_{app} = 0.8 V nm^{-1}. The line is an Arrhenius fitting with a slope of 23 meV. (d) Electric field dependent BLG band gap E_{gap}. The error bars are the standard errors of the fitted slopes in Figure 1c. The dashed lines indicate the linear relationship between E_{gap} and the electric field, and the deviation near zero field is likely due to resistance contributions unrelated to the gap.

First, we characterize the dependence of BLG channel resistance at 100 K as a function of top gate voltage (V_t) and bottom gate voltage (V_b) using four-point resistance measurements (current applied between E1 and E4 while measuring the voltage between E2 and E3). All measurements are performed at 100 K unless otherwise noted. The result is plotted in Figure 1b as a function of carrier density (n, positive for electrons) and perpendicular electric field (D_{app}), which are related to V_b and V_t, by $n = \frac{\varepsilon_t \varepsilon_0}{d_t e}(V_t - V_{t0}) + \frac{\varepsilon_b \varepsilon_0}{d_b e}(V_b - V_{b0})$ and $D_{app} = \frac{1}{2}[-\frac{\varepsilon_t}{d_t}(V_t - V_{t0}) + \frac{\varepsilon_b}{d_b}(V_b - V_{b0})]$, where ε_t (ε_b) is the relative dielectric constant of h-BN (SiO_2), ε_0 is the vacuum dielectric constant, d_t (d_b) is the thickness of h-BN (SiO_2), e is the electron charge, V_{t0} (V_{b0}) is the effective top (bottom) gate voltage offset due to initial environmental doping [31]. Detailed calculations are shown in SM section S2 [36]. The key features of the data (Figure 1b) are a resistance maximum as a function of n, which occurs at the charge neutrality point (CNP) located at $n = 0$ cm^{-2}. This resistance maximum, R_{peak}, increases with electric field D_{app} due to the opening of a band gap. In addition to this feature, there is also a broader resistance maximum that appears as a diagonal ridge. This is due to resistance contributions in the regions of BLG outside of the top gate (thus modulated only by the bottom gate), which is outside of our region of interest. Returning to the main peak features, by measuring the temperature dependence of R_{peak} for a constant value of D_{app}, we extract E_{gap} by Arrhenius fitting (Figure 1c) [30]. By repeating this for different values of D_{app}, we obtain the dependence of band gap on electric field (Figure 1d). The maximum E_{gap} is about 50 meV within the electric field applied, which is consistent with previous reports [31].

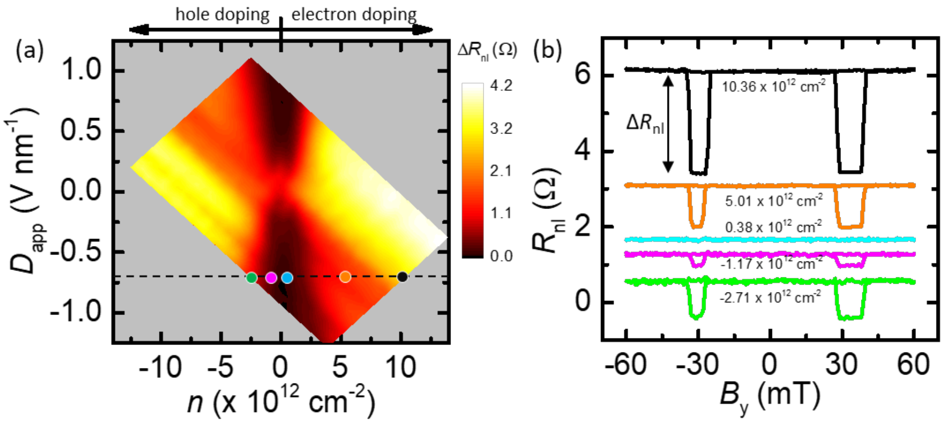

FIG. 2. (a) Electric field and carrier density dependence of non-local spin signal ΔR_{nl}. (b) Non-local magnetoresistance R_{nl} as a function of B_y at $D_{\text{app}} = -0.7$ V nm^{-1} for various carrier densities (dashed line in Figure 2a). Measurements are performed at 100 K.

Turning our attention to spin transport, Figure 2 shows the spin transport signal ΔR_{nl} as a function of n and D_{app}. This is obtained using the non-local spin transport geometry: a current source I_{inj} applied between the electrodes E1 and E2 (spin injector) creates spins in the BLG beneath E2 which subsequently diffuse toward the spin detector E3, where it is measured as a voltage signal V_{nl} across electrodes E3 and E4. The four-terminal non-local resistance is defined as $R_{\text{nl}} = V_{\text{nl}}/I_{\text{inj}}$. Figure 2b shows a detailed scan of R_{nl} as a function of magnetic field B_y at $D_{\text{app}} = -0.7$ V nm^{-1} for different n, corresponding to the five points in Figure 2a. A hysteretic jump is observed as Co electrode magnetizations switch between parallel (high R_{nl}) and antiparallel (low R_{nl}) configurations. The presence of these jumps indicates spin transport in the BLG, and the non-local spin signal is defined as $\Delta R_{\text{nl}} = R_{\text{nl}}$ (parallel) – R_{nl} (antiparallel), as indicated by the arrow in Figure 2b. The detailed dependence of ΔR_{nl} on n and D_{app} is summarized in Figure 2a. The main feature is that ΔR_{nl} decreases while approaching the CNP and further decreases to zero with an applied D_{app}.

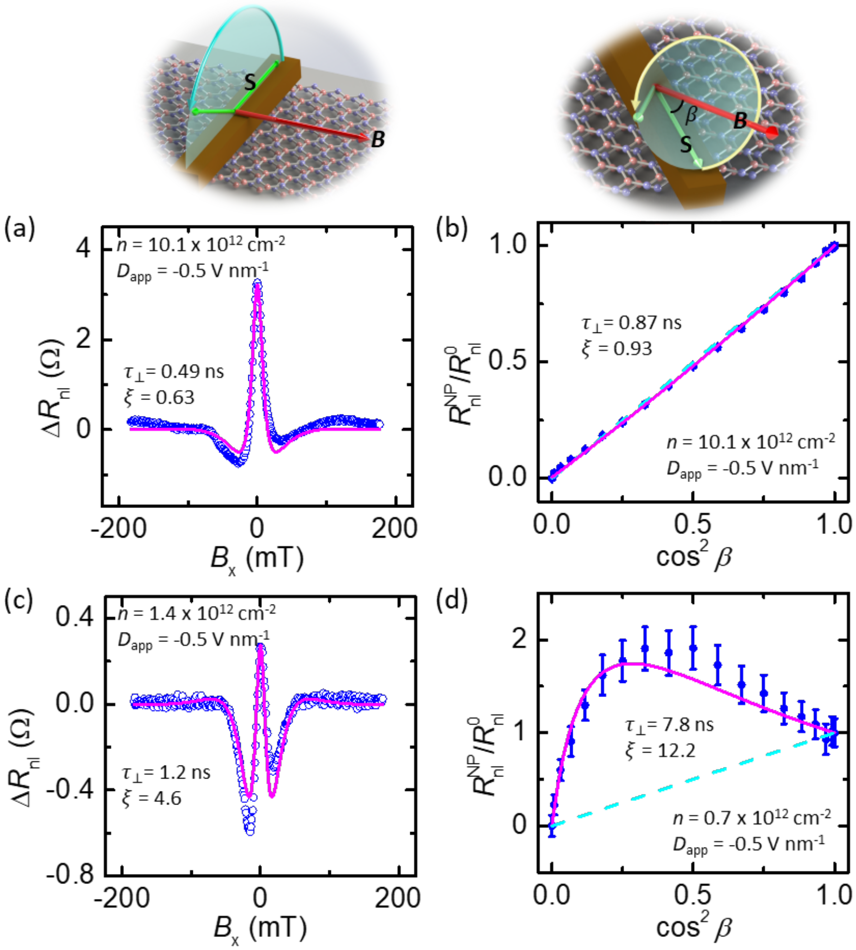

FIG. 3. (a) and (c) In-plane magnetic field Hanle at $D_{\mathrm{app}} = -0.5$ V nm^{-1} for two different carrier densities. (b) and (d) Oblique Hanle at $D_{\mathrm{app}} = -0.5$ V nm^{-1} for two different carrier densities. Blue dots are data, the magenta curve is the fit and the cyan dashed line is the guideline of y = x (no anisotropy). The error bars are standard deviations of the measured data points. Measurements are performed at 100 K.

To understand this strong tunability of ΔR_{nl}, we perform both in-plane magnetic field Hanle and oblique Hanle measurements. The in-plane magnetic field Hanle measurement is done by applying a magnetic field B_{x} along x direction so that spins precess in the y-z plane as it transports across the BLG [25] (see Figure 3a inset). Oblique Hanle measurements are done by applying a magnetic field $\boldsymbol{B} = (B_{\mathrm{y}},B_{\mathrm{z}})$ in y-z plane with various angles β between magnetic field $\boldsymbol{B}$ and Co electrode so that spins precess about a cone as it transports across the BLG [39-41] (see Figure 3b inset). Because the precession involves both in-plane and out-of-plane spin components, these spin precession measurements can be used to determine the spin lifetime anisotropy ξ.

Figures 3a and 3b show the results for in-plane magnetic field Hanle and oblique Hanle, respectively, for high electron density, n =10.1 × 10^{12} cm^{-2}. In this regime, the Hanle curves are similar to those observed typically in graphene spin valves without substantial spin lifetime anisotropy [4,39]. For the in-plane magnetic field Hanle (Figure 3a), the curve has a maximum spin signal at zero field which decreases with increasing B_x due to precessional dephasing. The small negative lobes are typical of Hanle curves when the channel length (here L = 7 μm) is longer than the spin diffusion length. For quantitative analysis of the data, we employ a one-dimensional spin diffusion model that allows for different values of in-plane ($\tau_\parallel$) and out-of-plane ($\tau_\perp$) spin lifetime (see SM section S3 for details [36]). The fitting (magneta curve) yields a spin lifetime anisotropy value of ξ = 0.63, with corresponding spin lifetime values of $\tau_\parallel$ = 0.77 ns and $\tau_\perp$ = 0.49 ns. For anisotropy ξ on the order of 1 or less, the oblique Hanle method yields more reliable values. Figure 3b summarizes the key data obtained from a series of oblique Hanle curves to determine ξ. Each data point comes from an oblique Hanle curve taken for a different value of β (see SM section S4 for details [36]). This plots the non-precessing component of spin signal (R_{nl}^{NP}) normalized by the in-plane spin signal (R_{nl}^{0}) as a function of $cos^2\beta$. For ξ = 1, the value of R_{nl}^{NP} will vary linearly with $cos^2\beta$ (specifically, $R_{nl}^{NP}/R_{nl}^{0} = cos^2\beta$), while the R_{nl}^{NP}/R_{nl}^{0} vs. $cos^2\beta$ curve will lie *below* the linear curve for ξ < 1, and the R_{nl}^{NP}/R_{nl}^{0} vs. $cos^2\beta$ curve will lie *above* the linear curve for ξ > 1. Figure 3b shows that the measured R_{nl}^{NP}/R_{nl}^{0} (blue dots) as a function of $cos^2\beta$ lies slightly below the linear curve (dashed cyan line). A quantitative fit (magneta line) yields a value of ξ = 0.93, with corresponding values of $\tau_\parallel$ = 0.94 ns and $\tau_\perp$ = 0.87 ns. Comparing the results from in-plane magnetic field Hanle (ξ = 0.63) and oblique Hanle (ξ = 0.93), we consider the latter method as more reliable quantitatively, while the former method is more useful for rapidly identifying ξ from a single spin-precession scan. As discussed in SM section S3, there are four fitting parameters (effective spin polarization P, spin diffusion coefficient D_s, in-plane spin lifetime $\tau_\parallel$ and spin lifetime anisotropy ξ) using in-plane magnetic field Hanle while there is only one fitting parameter ξ using oblique Hanle (P is cancelled by using the ratio R_{nl}^{NP}/R_{nl}^{0}, while D_s and $\tau_\parallel$ are extracted from out-of-plane magnetic field Hanle).

Moving closer to the CNP, we observe a dramatically different shape for the in-plane magnetic field Hanle curve, as shown in Figure 3c for n = 1.4 x 10^{12} cm^{-2} and D_{app} = - 0.5 V nm^{-1}. Here, the negative lobes become even larger than the peak at zero magnetic field and is very different from any Hanle curve without spin lifetime anisotropy. Such a curve was first reported by Ghiasi *et al.* [25] for graphene-MoSe$_2$ heterostructures and occurs when $\xi \gg 1$. Fitting this curve (magneta line) yields a large spin lifetime anisotropy value of ξ = 4.6, with corresponding spin lifetime values of $\tau_\parallel$ = 0.26 ns and $\tau_\perp$ = 1.20 ns. Figure 3d shows results for oblique Hanle measurements taken for n = 0.7 x 10^{12} cm^{-2} and D_{app} = -0.5 V nm^{-1}. Notably, the R_{nl}^{NP}/R_{nl}^{0} vs. $cos^2\beta$ curve is substantially higher than the linear curve (dashed cyan line), which is indicative of a large ξ. A quantitative fit yields a large spin lifetime anisotropy value of $\xi = 12.2$, with corresponding spin lifetime values of $\tau_{\parallel} = 0.64$ ns and $\tau_{\perp} = 7.8$ ns. This strong spin lifetime anisotropy $\xi = 12.2$ in BLG is comparable to monolayer graphene-TMDC heterostructures [25,26], but with a much longer spin lifetime.

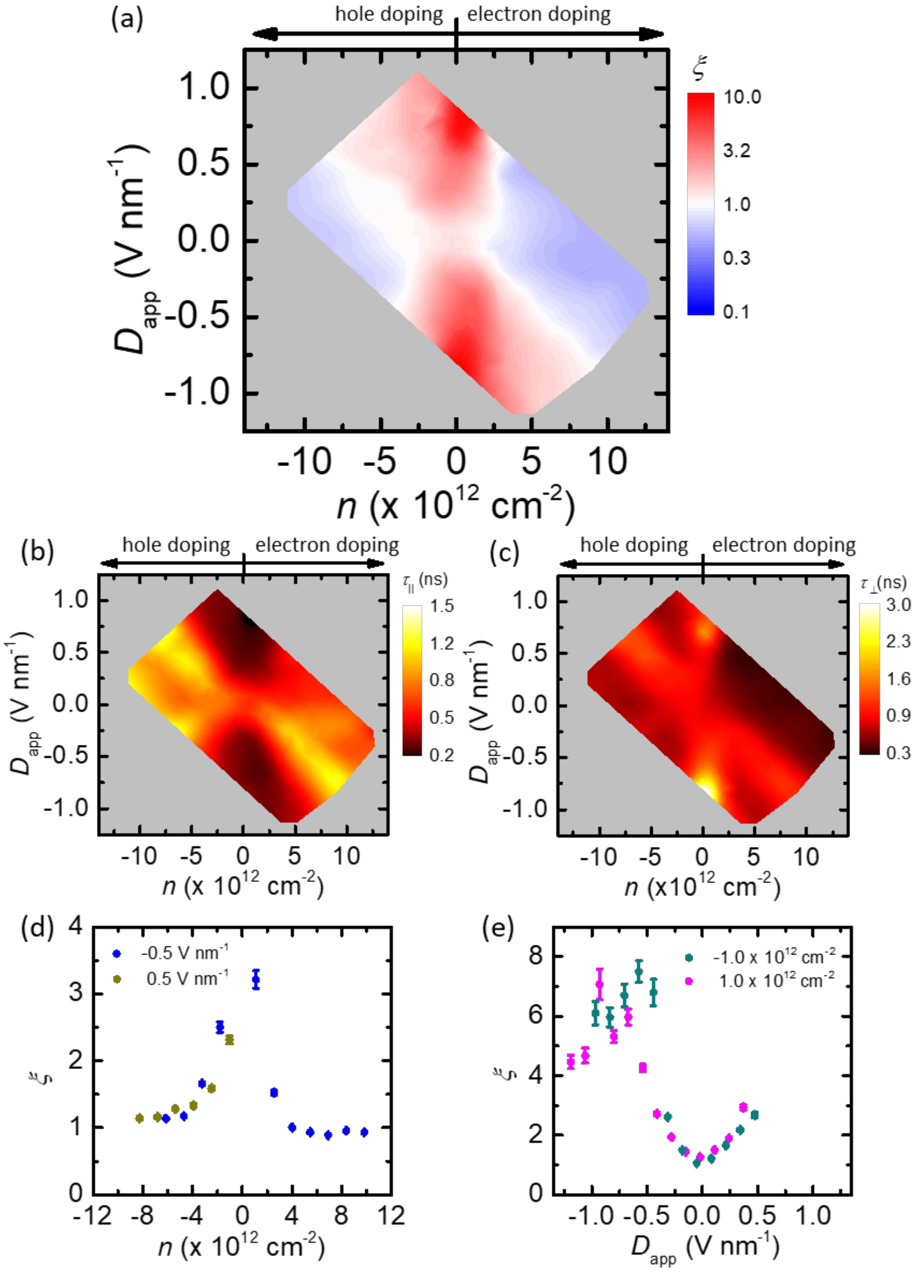

FIG. 4. (a-c) Electric field and carrier density dependence of spin lifetime anisotropy, in-plane spin lifetime, and out-of-plane spin lifetime, respectively, extracted from in-plane magnetic field Hanle measurements. (d, e) Spin lifetime anisotropy as a function of carrier density and electric field, respectively, extracted from oblique Hanle measurements. Measurements are performed at 100 K.

To understand the detailed role of carrier density and electric field on spin lifetime anisotropy, we utilize in-plane magnetic field Hanle measurements to efficiently generate 2D maps of ξ, $\tau_{\parallel}$ and $\tau_{\perp}$ as a function of n and D_{app} (Figures 4a, 4b, and 4c), and then perform selective line cuts using oblique Hanle measurements to quantitatively assess the variations with n (Figure 4d) and D_{app} (Figure 4e). A number of trends are observed. As shown in Figure 4a, it is clear the carrier density needs to be near charge neutrality (n = 0 cm^{-2}) and an electric field must be applied in order to have a large ξ. To understand whether the large anisotropy is due to an increase of $\tau_{\perp}$ and/or a decrease of $\tau_{\parallel}$, we consider the maps in Figures 4b and 4c. Starting at the CNP and D_{app} = 0 V nm^{-1}, increasing the magnitude of D_{app} leads to both a reduction of $\tau_{\parallel}$ (Figure 4b) and an enhancement of $\tau_{\perp}$ (Figure 4c). For the $\tau_{\parallel}$ map, it is interesting to note that this resembles the map of the non-local spin signal in Figure 2a, which makes sense because the non-local spin transport is for spins oriented in-plane. For the $\tau_{\perp}$ map, we notice a diagonal ridge similar to that observed in Figure 1b. This is also likely to originate from regions of the graphene with only bottom gate and is thus outside the primary region of interest. Fortunately, similar features appear for both $\tau_{\parallel}$ and $\tau_{\perp}$ so they have only minor impact on the ξ map. Turning to the oblique Hanle line cuts, the dependence of ξ on carrier density for different fixed electric fields shows a large value near charge neutrality with applied D_{app} = -0.5 V nm^{-1} or 0.5 V nm^{-1} and a reduction to $\xi \sim 1$ with increasing carrier density (Figure 4d). Figure 4e shows the dependence of ξ on electric field D_{app} for carrier densities n = -1.0 x 10^{12} cm^{-2} and 1.0 x 10^{12} cm^{-2}. Toward negative D_{app}, the ξ first increases with magnitude of electric field, then saturates around 0.5 V nm^{-1} and eventually decreases. This is observed for both the electron and hole doping [42].

This electric field and carrier density dependence of the spin lifetime anisotropy can be qualitatively understood using a simple phenomenological model. Since the low-energy physics is controlled by the electronic band structure of BLG near zone corner K and K' [32,33], as schematically shown in Figure 5a, the out-of-plane spin lifetime $\tau_{\perp}$ should increase with the out-of-plane spin polarization $\langle S_{\mathrm{Z}} \rangle$ at K and K'. At finite temperature, based on the Fermi-Dirac distribution of carriers in the spin-split low energy bands of BLG close to the K and K' points, we have

$$\langle S_{\mathrm{Z}} \rangle \propto \pm \left(-\frac{1}{Exp\left[\frac{\frac{E_{\mathrm{gap}}}{2}+2\lambda_{\mathrm{I}}-\mu}{k_{\mathrm{B}}T}\right]+1} + \frac{1}{Exp\left[\frac{\frac{E_{\mathrm{gap}}}{2}-\mu}{k_{\mathrm{B}}T}\right]+1} + \frac{1}{Exp\left[\frac{-\frac{E_{\mathrm{gap}}}{2}-\mu}{k_{\mathrm{B}}T}\right]+1} - \frac{1}{Exp\left[\frac{-\frac{E_{\mathrm{gap}}}{2}-2\lambda_{\mathrm{I}}-\mu}{k_{\mathrm{B}}T}\right]+1} \right) \quad (1),$$

where + (-) corresponds to K (K') valley, λ_{I} is the intrinsic SOC, μ is the chemical potential (using the middle of the gap as zero potential), and T is temperature. Figure 5b is the plot of out-of-plane spin polarization $\langle S_{\mathrm{Z}} \rangle$, with E_{gap} = 60 D_{app} meV (D_{app} in units of V nm^{-1}) extracted from Figure 1d, λ_{I} = 12 μeV,

T = 100 K and μ = 1 meV. $\langle S_Z \rangle$ first increases with electric field D_{app}, then saturates and decreases eventually, implying a similar D-dependence for the out-of-plane spin lifetime $\tau_{\perp}$. This toy model without detailed calculation well explains the observed electric field dependence of the spin lifetime anisotropy (Figure 4e). In addition, $\langle S_Z \rangle$ will decay quickly moving away from the K or K' points in momentum space due to rapid decrease of λ_{I}, resulting in the decrease of spin lifetime anisotropy with increasing carrier density, as observed experimentally (Figure 4d). These results are consistent with Dyakonov-Perel spin relaxation in the presence of out-of-plane spin-orbit fields, which will reduce the in-plane spin lifetime (Figure 4b) by inducing additional precessional dephasing, while also stabilizing the out-of-plane spins against precessional dephasing for enhanced spin lifetimes (Figure 4c).

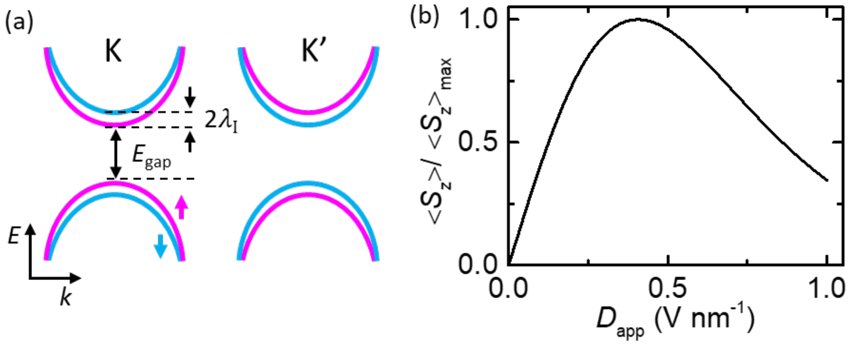

FIG. 5. (a) Schematic drawing of the BLG band structure with applied electric field. Red (blue) curves represent spin up (down) bands. (b) Electric field dependence of normalized $<S_Z>$ with E_{gap} = 60 D_{app} meV (D_{app} in units of V nm^{-1}), λ_{I} = 12 μeV, T = 100 K and μ = 1 meV.

In conclusion, we have observed large and tunable spin lifetime anisotropy in dual-gated BLG spin valves. Investigating the dependence on electric field and carrier density, we find spin lifetime anisotropy as strong as ξ = 12.2 with an out-of-plane spin lifetime up to 7.8 ns. Near the CNP, the spin lifetime anisotropy first increases with electric field, then saturates and eventually decreases, which is explained using a simple model of the spin-valley coupled band structure of BLG. Our results demonstrate the potential for highly tunable spintronic devices based on dual-gated 2D materials.

Note. During preparation of this manuscript, we became aware of a similar result using single-gated BLG [43].

ACKNOWLEDGEMENTS

We acknowledge technical assistance from Jyoti Katoch, Simranjeet Singh, and Dongying Wang. Funding for this research was provided by the Center for Emergent Materials: an NSF MRSEC under award number DMR-1420451.

REFERENCES

[1] D. Huertas-Hernando, F. Guinea, and A. Brataas, *Phys. Rev. B* **74**, 155426 (2006).

[2] H. Min, J. E. Hill, N. A. Sinitsyn, B. R. Sahu, L. Kleinman, and A. H. MacDonald, *Phys. Rev. B* **74**, 165310 (2006).

[3] M. Gmitra, S. Konschuh, C. Ertler, C. Ambrosch-Draxl, and J. Fabian, *Phys. Rev. B* **80**, 235431 (2009).

[4] W. Han, R. K. Kawakami, M. Gmitra, and J. Fabian, *Nat. Nanotechnol.* **9**, 794 (2014).

[5] M. Drögeler, C. Franzen, F. Volmer, T. Pohlmann, L. Banszerus, M. Wolter, K. Watanabe, T. Taniguchi, C. Stampfer, and B. Beschoten, *Nano Lett.* **16**, 3533 (2016).

[6] J. Ingla-Aynés, R. J. Meijerink, and B. J. van Wees, *Nano Lett.* **16**, 4825 (2016).

[7] M. H. D. Guimarães, P. J. Zomer, J. Ingla-Aynés, J. C. Brant, N. Tombros, and B. J. van Wees, *Phys. Rev. Lett.* **113**, 086602 (2014).

[8] S. Datta and B. Das, *Appl. Phys. Lett.* **56**, 665 (1990).

[9] G. Salis, Y. Kato, K. Ensslin, D. C. Driscoll, A. C. Gossard, and D. D. Awschalom, *Nature* **414**, 619 (2001).

[10] A. Soumyanarayanan, N. Reyren, A. Fert, and C. Panagopoulos, *Nature* **539**, 509 (2016).

[11] C. Tang, B. Cheng, M. Aldosary, Z. Wang, Z. Jiang, K. Watanabe, T. Taniguchi, M. Bockrath, and J. Shi, *APL Mater.* **6**, 026401 (2018).

[12] Z. Wang, C. Tang, R. Sachs, Y. Barlas, and J. Shi, *Phys. Rev. Lett.* **114**, 016603 (2015).

[13] P. Wei, S. Lee, F. Lemaitre, L. Pinel, D. Cutaia, W. Cha, F. Katmis, Y. Zhu, D. Heiman, J. Hone, J. S. Moodera, and C.-T. Chen, *Nat. Mater.* **15**, 711 (2016).

[14] J. C. Leutenantsmeyer, A. A. Kaverzin, M. Wojtaszek, and B. J. van Wees, *2D Mater.* **4**, 014001 (2016).

[15] S. Singh, J. Katoch, T. Zhu, K.-Y. Meng, T. Liu, J. T. Brangham, F. Yang, M. E. Flatté, and R. K. Kawakami, *Phys. Rev. Lett.* **118**, 187201 (2017).

[16] J. Xu, S. Singh, J. Katoch, G. Wu, T. Zhu, I. Zutic, and R. K. Kawakami, *arXiv:1802.07790* (2018).

[17] Y. K. Luo, J. Xu, T. Zhu, G. Wu, E. J. McCormick, W. Zhan, M. R. Neupane, and R. K. Kawakami, *Nano Lett.* **17**, 3877 (2017).

[18] A. Avsar, D. Unuchek, J. Liu, O. L. Sanchez, K. Watanabe, T. Taniguchi, B. Özyilmaz, and A. Kis, *ACS Nano* **11**, 11678 (2017).

[19] W. Yan, O. Txoperena, R. Llopis, H. Dery, L. E. Hueso, and F. Casanova, *Nat. Commun.* **7**, 13372 (2016).

[20] A. Dankert and S. P. Dash, *Nat. Commun.* **8**, 16093 (2017).

[21] Z. Wang, D. K. Ki, H. Chen, H. Berger, A. H. MacDonald, and A. F. Morpurgo, *Nat. Commun.* **6**, 8339 (2015).

[22] B. Yang, M.-F. Tu, J. Kim, Y. Wu, H. Wang, J. Alicea, R. Wu, M. Bockrath, and J. Shi, *2D Mater.* **3**, 031012 (2016).

[23] Z. Wang, D.-K. Ki, J. Y. Khoo, D. Mauro, H. Berger, L. S. Levitov, and A. F. Morpurgo, *Phys. Rev. X* **6**, 041020 (2016).

[24] B. Yang, M. Lohmann, D. Barroso, I. Liao, Z. Lin, Y. Liu, L. Bartels, K. Watanabe, T. Taniguchi, and J. Shi, *Phys. Rev. B* **96**, 041409 (2017).

[25] T. S. Ghiasi, J. Ingla-Aynés, A. A. Kaverzin, and B. J. van Wees, *Nano Lett.* **17**, 7528 (2017).

[26] L. A. Benítez, J. F. Sierra, W. S. Torres, A. Arrighi, F. Bonell, M. V. Costache, and S. O. Valenzuela, *Nat. Phys.* **14**, 303 (2018).

[27] M. Gmitra, D. Kochan, P. Hogl, and J. Fabian, *Phys. Rev. B* **93**, 155104 (2016).

[28] M. Gmitra and J. Fabian, *Phys. Rev. Lett.* **119**, 146401 (2017).

[29] J. Y. Khoo, A. F. Morpurgo, and L. Levitov, *Nano Lett.* **17**, 7003 (2017).

[30] J. B. Oostinga, H. B. Heersche, X. Liu, A. F. Morpurgo, and L. M. K. Vandersypen, *Nat. Mater.* **7**, 151 (2008).

[31] Y. Zhang, T.-T. Tang, C. Girit, Z. Hao, M. C. Martin, A. Zettl, M. F. Crommie, Y. R. Shen, and F. Wang, *Nature* **459**, 820 (2009).

[32] R. van Gelderen and C. M. Smith, *Phys. Rev. B* **81**, 125435 (2010).

[33] S. Konschuh, M. Gmitra, D. Kochan, and J. Fabian, *Phys. Rev. B* **85**, 115423 (2012).

[34] D. Xiao, G.-B. Liu, W. Feng, X. Xu, and W. Yao, *Phys. Rev. Lett.* **108**, 196802 (2012).

[35] S. Singh, J. Katoch, T. Zhu, R. J. Wu, A. S. Ahmed, W. Amamou, D. Wang, K. A. Mkhoyan, and R. K. Kawakami, *Nano Lett.* **17**, 7578 (2017).

[36] See Supplemental Material, which includes refs [31,37,38,40] and sections on device fabrication, determination of carrier density and electric field, spin diffusion model for in-plane magnetic field Hanle and oblique Hanle, oblique Hanle data, and data from an additional sample.

[37] M. Johnson and R. H. Silsbee, *Phys. Rev. B* **37**, 5312 (1988).

[38] E. Sosenko, H. Wei, and V. Aji, *Phys. Rev. B* **89**, 245436 (2014).

[39] B. Raes, J. E. Scheerder, M. V. Costache, F. Bonell, J. F. Sierra, J. Cuppens, J. van de Vondel, and S. O. Valenzuela, *Nat. Commun.* **7**, 11444 (2016).

[40] B. Raes, A. W. Cummings, F. Bonell, M. V. Costache, J. F. Sierra, S. Roche, and S. O. Valenzuela, *Phys. Rev. B* **95**, 085403 (2017).

[41] T. Zhu and R. K. Kawakami, *Phys. Rev. B* **97**, 144413 (2018).

[42] Due to the limited magnetic field orientation of the 2-axis vector magnet, it is impossible to perform in-plane and out-of-plane magnetic field Hanle at the same time. The sample was heated to room temperature and remounted in between the in-plane magnetic field Hanle and oblique Hanle measurements, leading to a shift of the gate voltage offsets. Unfortunately, the trend for positive D_{app} could not be tested to similarly high values due to this gate voltage shift after sample reload.

[43] J. C. Leutenantsmeyer, J. Ingla-Aynés, J. Fabian, and B. J. van Wees, *arXiv:1805.12420* (2018).